トピックス

# Atomic and Electronic Structures of Epitaxial Thin Iron Oxide Films on Pt(111)

**Yong Q. CAI**

*Japan Science and Technology Corporation, and*
*Institute for Solid State Physics, University of Tokyo**

Single-crystal metal oxide thin films grown epitaxially on conducting substrates have recently attracted increased attention in surface science studies of catalytic processes and of the electronic and magnetic properties of metal oxides due to a number of advantages compared to their bulk counterparts: Notably they offer well-controlled surface conditions (cleanliness, stoichiometry and crystalline order) and, for insulating oxides, a solution to the electrostatic charging problem associated with the use of analytical techniques involving charged particles (e.g., various electron spectroscopies and scanning tunnelling microscopy, etc.). It has recently been shown that well-ordered, thin iron oxide films can be prepared epitaxially on clean Pt(111) surfaces. The atomic and electronic structures of these thin oxide films have been studied using various techniques, including scanning tunnelling microscopy, low-energy electron diffraction, near-edge x-ray absorption fine structure and angle-resolved photoelectron spectroscopy with synchrotron radiation. The present status of understanding of the atomic and electronic structures of these thin iron oxide films is reviewed.

## 1. Introduction

The surfaces of metal oxides play a crucial role in many of the applications of these technologically important materials, which range from catalysts to corrosion-resistive coatings to gas sensors. Yet, our understanding of the atomic and electronic structure of these metal oxide surfaces lags far behind that of metal and semiconductor surfaces[1]. The central problem responsible for this state of affairs lies in the difficulty in the preparation of well-defined surfaces of metal oxides for surface science studies. Their brittle nature and the difficulty in maintaining the oxygen concentration during surface cleaning processes of bulk single crystals in ultra-high vacuum (UHV), often lead to disordered and/or non-stoichiometric surfaces by conventional means (e.g., cleaving, filing, sputtering and annealing). For insulating oxides, the surface electrostatic charging effect causes additional problems when analytical techniques involving the emission or absorption of charged particles are used. In contrast, the recent development of growing single-crystal metal-oxide thin films epitaxially on conducting substrates appears to have solved these problems[2]. The cleanliness, stoichiometry and crystalline order of the surface of these thin oxide films can be well controlled, and yet structurally and chemically they are found to be identical with their bulk counterparts[3-9]. Furthermore, for insulating oxides the electrostatic charges can be dissipated via the conducting substrate. These thin oxide films therefore provide new opportunities for spectroscopic and microscopic studies of the electronic and atomic structures of metal oxides, which is a prerequisite for understanding the physical principles governing their rich electrical and magnetic properties[10,11]. Moreover, they can be used for studying the surface chemistry of metal oxides which is in turn important for addressing the issues in metal-oxidebased catalysis[12].

Ordered metal oxide thin films can be prepared either by oxidizing the surface of the corresponding metal single crystals, as has been done for example for Ni and Cr[2], or by growing epitaxial oxide films onto dissimilar substrates via metal deposition and simultaneous or subsequent oxidation[3,8]. The former approach may produce films with a large number of defects if the lattice mismatch between the metal and the corresponding oxide is large. The latter approach offers more flexibility as quite often an inner, conducting substrate with a commensurate lattice constant may be chosen depending on the oxide to be grown. In this regard, well-ordered, thin (< 100 Å) $Al_2O_3$ films and several phases of iron oxide (FeO, $Fe_3O_4$ and $\alpha$-$Fe_2O_3$) films have been successfully grown on Ta(110)[8] and Pt(111)[3], respectively. Ordered $Al_2O_3$ thin films have also been reported to

* Institute for Solid State Physics, University of Tokyo 7-22-1, Roppongi, Minato-ku, Tokyo 106-8666, Japan
TEL 03-3478-6811(ext. 5676) FAX 03-3401-5169 e-mail cai@surface.issp.u-tokyo.ac.jp

grow on alloy NiAl(110) surface by oxidation[7]. It has also been shown that well-ordered, thicker (>100 Å) $Fe_3O_4$ and $\alpha$-$Fe_2O_3$ films with different orientations can be grown by oxygen-plasma-assisted molecular-beam epitaxy on MgO and $\alpha$-$Al_2O_3$ substrates[9].

In the present paper, we will concentrate on the iron oxide films grown on Pt(111) and review the present understanding of their atomic and electronic structures. The aim is not to exhaust the literature of related studies, but rather to give an example of how improved surface conditions may lead to new information and understanding, particularly with regard to the electronic structure of metal oxides, from well established experimental techniques such as angle-resolved photoemission. The rest of the paper will be organized as follows: Section II describes the growth of the iron oxide films; Section III discusses briefly the surface structure characterized by scanning tunnelling microscopy (STM) and low-energy electron diffraction (LEED); Section IV is devoted to the electronic structure, emphasizing that of the $Fe_3O_4$ multilayer, as obtained using angle-resolved photoemission in conjunction with synchrotron radiation. A summary and outlook are presented in Section V.

## 2. Thin Film Growth

The growth of the iron oxide thin films has been described in detail by Weiss[13] and by Ritter et al[14], and may be summarized in **Fig. 1**. The process begins with the cleaning of the Pt(111) substrate by repeated cycles of 1-keV $Ar^+$-ion bombardment and subsequent annealing at ~1100°C until it displays a sharp 1×1 LEED pattern (**Fig. 2(a)**) and no signs of contamination as judged by Auger electron or photoelectron spectroscopies. A submonolayer of iron is then deposited onto the clean Pt(111) surface at room temperature. The iron evaporation is achieved through resistive heating of a tungsten wire with a pure iron wire wrapped around it. This submonolayer iron film is then oxidized for 2 mins in a $1\times10^{-6}$ mbar oxygen partial pressure with an oxidation temperature depending on the thickness of the oxide film: Up to 1 monolayer coverage (equivalent to one Fe–O bilayer) the oxidation temperature is always at 730°C; above 1 monolayer the film is oxidized at a temperature between 600–650°C. To increase the film thickness this deposition and oxidation cycle is repeated.

Throughout the growth process, characteristic LEED patterns are observed which have been found to be a good indicator of the thickness and the phase of the iron oxide film[13,14]. These LEED patterns are shown in **Fig. 2(b)–(d)**. Films with a thickness of up to 2 monolayers exhibit a hexagonal LEED pattern similar to that shown in **Fig. 2(b)**, in which every integer-order spot is surrounded by six satellite spots. The satellite spots are caused by a coincidence structure between the Pt substrate and the iron oxide layer which will be discussed further in the next Section. For coverages of up to 2 monolayers, only the iron oxide phase FeO with the (111) surface orientation grows layer-by-layer on the Pt(111) surface. For coverages above 2 monolayers, $Fe_3O_4$ (111) islands begin to form on the FeO layer, and eventually

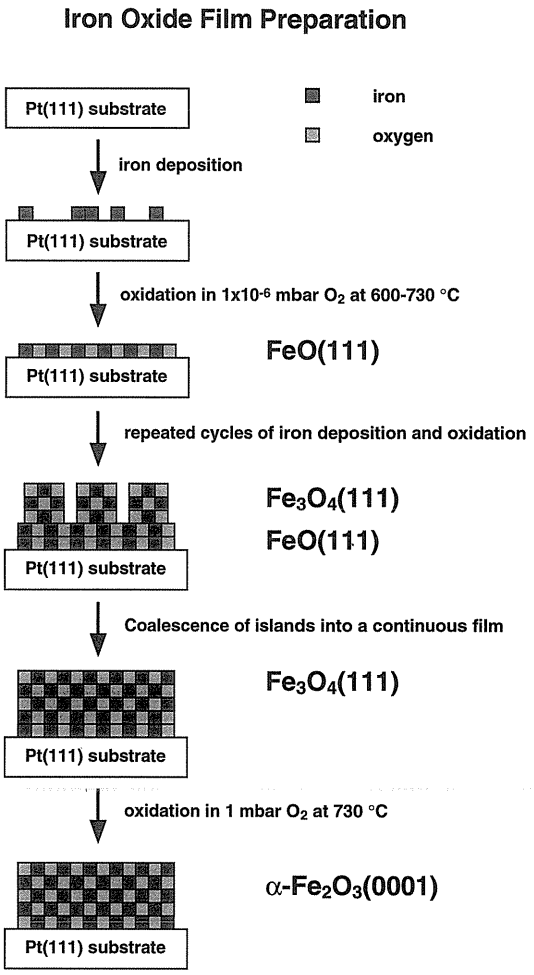


Figure 1. Schematic diagram showing the growth process of the iron oxide films on Pt(111).

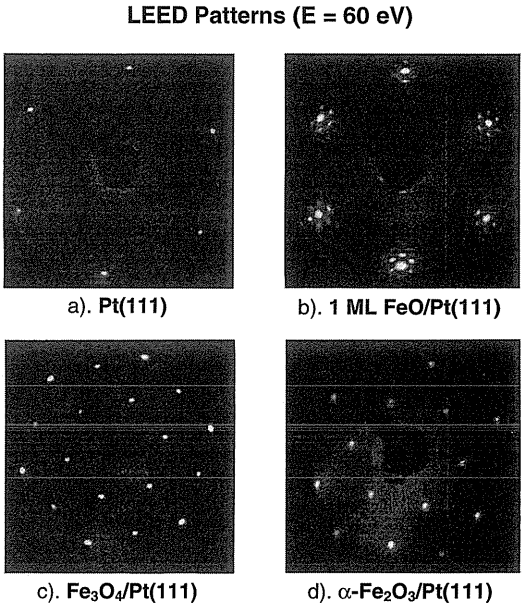


Figure 2. Low energy electron diffraction (LEED) patterns for the surface of (a) clean Pt(111), (b) 1 monolayer FeO film on Pt(111), (c) multilayer $Fe_3O_4$(111) film, and (d) multilayer $\alpha$-$Fe_2O_3$(0001) film. From Ref. 13.

coalesce to give a continuous film with increasing coverage. By this time the satellite spots have disappeared and a new $2\times2$ LEED pattern, characteristic of the $Fe_3O_4(111)$ surface, is observed (**Fig. 2(c)**).

The last phase of the iron oxide film, namely $\alpha$-$Fe_2O_3$ (0001), requires oxidation of the $Fe_3O_4$ multilayer film in 1-mbar partial pressure of oxygen at 730°C. A new $\sqrt{3}\times\sqrt{3}$-R30° LEED pattern (**Fig. 2(d)**) is observed after the oxidation, which corresponds to a hexagonal surface unit-cell characteristic of the $\alpha$-$Fe_2O_3$(0001) surface.

## 3. Structural Characterisation

The bulk atomic structure of the three phases of iron oxides mentioned above is well known[15]. FeO (wustite) crystallizes in the cubic sodium-chloride structure, $Fe_3O_4$ (magnetite) in the cubic inverse-spinel structure and $\alpha$-$Fe_2O_3$ (hematite) in the hexagonal corundum structure. The unreconstructed, iron-terminated (111) surface of FeO and $Fe_3O_4$ and the (0001) surface of $\alpha$-$Fe_2O_3$ are shown in **Fig. 3**. Neglecting slight lateral distortions away from a perfect hexagonal layer in the case of $Fe_3O_4$ and $\alpha$-$Fe_2O_3$, all three phases consist of hexagonally close-packed oxygen planes perpendicular to the [111] ([0001] in the case of $\alpha$-$Fe_2O_3$) axis with iron cations occupying different interstitial sites. Because of the difference in the iron cation positions, these ideal (111) ((0001) for $\alpha$-$Fe_2O_3$) surfaces have unit cells with dimensions of 3.04 Å for FeO, 5.94 Å for $Fe_3O_4$ and 5.02 Å for $\alpha$-$Fe_2O_3$, giving rise respectively to $1\times1$, $2\times2$ and $\sqrt{3}\times\sqrt{3}$-R30° surface superstructure cells with respect to the $1\times1$ cell of the oxygen planes of the three oxides. Hence the different LEED patterns observed from the three phases of the iron oxide film in the last section can be explained.

The satellite spots in the LEED pattern for the FeO film are due to multiple scatterings between the platinum substrate and the oxide overlayer, as there is a $9\times9$ coincidence structure on the Pt(111) surface[14]. This coincidence structure arises because of a 13% mismatch between the interatomic distance of the FeO(111) surface (3.11 Å) and that of the Pt(111) surface (2.77 Å) as determined from the positions of the integer-order spots in **Fig. 2(b)**[14]. A better example can be seen from **Fig. 4** in which a 55 Å × 55 Å STM image with atomic resolution and a structure model for the monolayer FeO film are shown[14]. The STM image exhibits a hexagonal surface structure with an atomic periodicity of about 3.1 Å representing the surface unit cell of the FeO film. The atomic features in the image correspond to the oxygen atom positions according to simulations based on electron-scattering quantum-chemistry theory[16]. An image height modulation showing a large hexagonal pattern is also visible. The periodicity of this modulation can be defined by

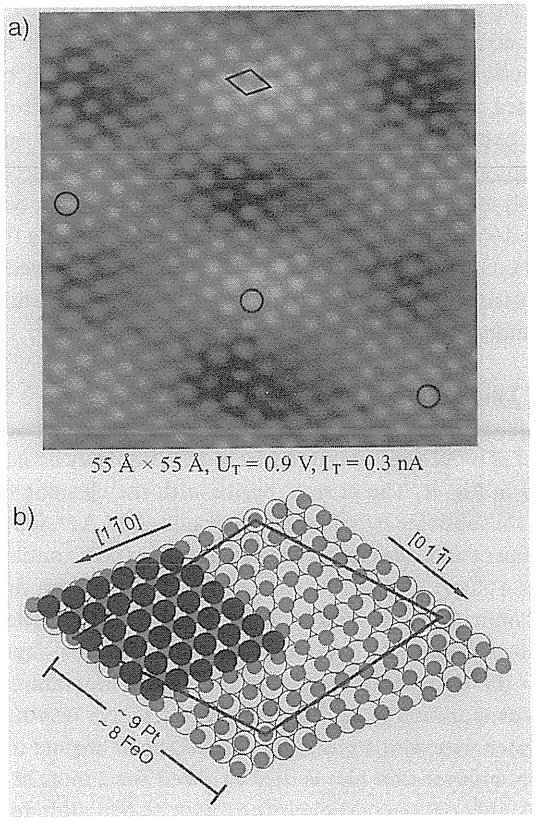


Figure 4. (a) Scanning tunnelling microscopy (STM) image of a monolayer FeO(111) film on Pt(111); (b) The corresponding surface model showing the $9\times9$ coincidence structure between the Pt substrate and the monolayer FeO(111) film. From Ref. 14.

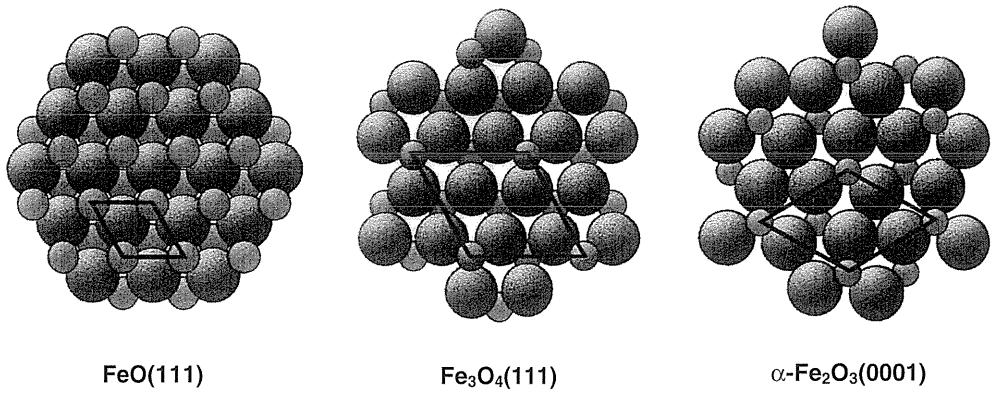


Figure 3. Ideal, bulk-terminated FeO(111), $Fe_3O_4$(111) and $\alpha$-$Fe_2O_3$(0001) surfaces.

the brightest atomic features (circled) in the STM image and is about 25 Å. This large hexagonal cell is rotated by about 11° relative to the 1 × 1 surface unit cell of the oxide layer as the brightest spots of this modulation are not on the same atomic row.

Consistent with both the STM image and photoelectron diffraction studies[17], the proposed model (**Fig. 4(b)**) consists of a laterally expanded oxygen-terminated FeO(111) bilayer on top of the Pt(111) surface. The iron atoms are separated by 3.1 Å and form rows that are rotated by 1.3° with respect to the underlying platinum atom rows along the [01$\bar{1}$] and [1$\bar{1}$0] directions, leading to a coincidence structure spanning 9 platinum atoms along the [01$\bar{1}$] direction and 3 along the [1$\bar{1}$0] direction. Each coincidence point marks the position where an iron atom is directly above a platinum atom. The unit cell of this coincidence structure, as determined from the model, is 25.4 Å in size and is rotated by 12.2° with respect to the 1 × 1 unit cell of the FeO(111) surface. This is in good agreement with the STM result.

There are more coincidence structures as the FeO(111) film grows into the second monolayer, which have been discussed in detail by Ritter et al[14]. They are all slightly laterally expanded (lattice constant from 3.09–3.15 Å) compared to bulk FeO (3.04 Å), but have the same interlayer distance as the bulk (2.5 Å)[5,14]. Furthermore, the surface is unreconstructed and contains few defects. This is surprising because being a polar surface, the (111) surface has a diverging surface free energy and should be unstable[2]. This ultrathin FeO film, as suggested by Ritter et al[14], must therefore be stabilized by an image dipole in the platinum substrate which compensates the dipole in the oxide overlayer.

The surface structure of the $Fe_3O_4$(111) multilayer film has been studied by dynamic LEED simulation[4]. The most favored surface structure of the multilayer $Fe_3O_4$(111) film is found to correspond to a strongly relaxed, unreconstructed bulk (111) termination, in which the surface contains one iron atom per 2 × 2 unit cell. This is illustrated in **Fig. 5**. Each of these surface iron atoms is bonded to three oxygen atoms underneath. The main features of the surface relaxation include: (1) a $\Delta = 0.42 \pm 0.18$ Å upward displacement of the surface oxygen atom labeled "A" (not bonded to a surface iron) with respect to the oxygen atoms labeled "B" (bonded to a surface iron), and (2) deviations in spacing between the second iron layer and the two oxygen planes formed by the "B" oxygen atoms above ($d_{12} = 0.83 \pm 0.05$ Å) and the oxygen atoms labeled "C" below ($d_{23} = 1.42 \pm 0.04$ Å) from the bulk value of 1.19 Å. The upward displacement of the "A" oxygen atoms, in particular, shortens the distance between the surface iron atoms and the "A" oxygen atoms, thereby reduces the electrostatic surface dipole of the unreconstructed termination and contributes to the stability of the surface. Of all the possible, unreconstructed (111) terminations of $Fe_3O_4$, this termination has the least number of dangling bonds. Inclusion of vacancies and other possible bulk terminations in the simulation did not significantly improve the agreement with the experimental results. Nevertheless, preliminary results from recent surface characterisation using STM[14,18] show that the surface contains oxygen defects, which is another important mechanism for lowering the surface free energy and stabilizing the polar $Fe_3O_4$(111) surface.

More recently, the surface structure of the $\alpha$-$Fe_2O_3$(0001) film has been studied by STM and *ab-initio* calculations using density functional theory[19]. Consistent with the observed six-fold symmetric LEED pattern, two different domains with iron and oxygen terminations, respectively, are observed on the surface of a film prepared at a $10^{-3}$ mbar oxygen partial pressure by STM. The calculations indicate that the surface would be oxygen terminated if it was oxidized in a high oxygen pressure, whereas an iron terminated surface would be produced if oxidation was performed in a low oxygen pressure environment.

## 4. Electronic Structure

So far, the electronic structure of the iron oxide films has been studied by x-ray absorption nearedge structure (XANES) and by core and valence level photoemission[5,20]. The former technique probes the unoccupied states, and is also a useful tool for determining the molecular bond length and orientation when combined with polarisation-depen-

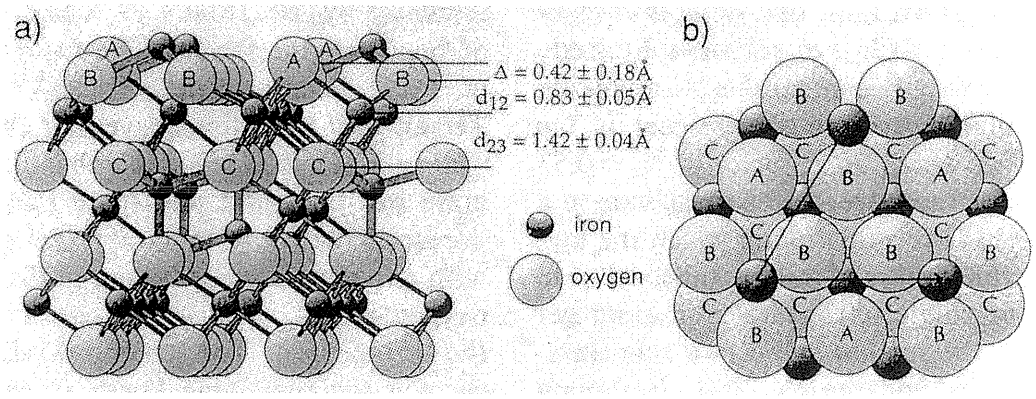


Figure 5. Surface structure model for the multilayer $Fe_3O_4$(111) film as determined by dynamic LEED simulations. From Ref. 4.

dent intensity variations obtained using polarized light from synchrotron radiation[21]. The bond length of the monolayer FeO film was determined in this way and found to be almost identical to that of bulk FeO single crystals[5]. The x-ray absorption near both the oxygen $K$ edge and the iron $L_{2,3}$ edges of the iron oxide films on Pt(111) produces spectral features that compare well with those obtained from bulk single-crystal samples[5]. This indicates that only single-phased iron oxide films are grown on the Pt(111) substrate under the conditions described in Section II.

On the other hand, photoemission has proven to be a powerful technique, especially in combination with tunable, polarized light produced by synchrotron radiation, for the study of occupied electronic structures of a wide range of systems[22]. In this regard, characteristic core-level photoemission spectra from the Fe 2$p$ and O 1$s$ states have been obtained from the three iron oxide films[5], which are essentially identical with those obtained from bulk single crystals, and offer further support for the correct chemical and structural identification of these iron oxide films. Furthermore, the valence electronic structure of the multilayer $Fe_3O_4$(111) film has been studied using angle-resolved photoemission in conjunction with synchrotron radiation[20]. New information is revealed compared to previous studies of bulk single crystals, which presumably is due to the improved surface quality of the iron oxide film. In the following, the results of this study will be discussed in some detail.

As stated earlier, $Fe_3O_4$, being a ferrimagnet, has the cubic inverse spinel structure. At room temperature the lattice is fcc and consists in a purely ionic model of a close-packed face-centered cube of $O^{2-}$ anions with two kinds of cations, $Fe^{2+}$ and $Fe^{3+}$, located in the interstitial sites of the anion lattice. Two cation sites exist in the crystal: One site designated $A$ is tetrahedrally coordinated to oxygen and is occupied only by $Fe^{3+}$ ions. The other site designated $B$ is octahedrally coordinated to oxygen and is occupied by equal numbers of $Fe^{2+}$ and $Fe^{3+}$ ions. At about 120 K ($T_v$), magnetite undergoes a phase transition, named after Verwey[23], in which the conductivity drops sharply by two orders of magnitude[24] and the crystallographic structure changes from cubic to monoclinic[25]. The high electrical conductivity of magnetite at room temperature is attributed to electron hopping between the $Fe^{2+}$ and the $Fe^{3+}$ ions occupying the $B$ site by theories based on the localized-electron point of view. The Verwey transition freezes these electrons and causes an ordering of the extra electron (compared to $Fe^{3+}$) at the $Fe^{2+}$ $B$ site at temperatures below $T_v$, although the precise ordering is still unclear[26]. The same phenomenon, however, can also be explained from band theory which considers the high conductivity as a natural consequence of the half-filled 3$d$ band of iron atoms located at the $B$ site. The Verwey transition is a result of a band splitting due to the increasing importance of electron-electron correlation and/or electron-phonon interactions at low temperatures[10].

This controversy is echoed by the debate over the interpretation of the valence-band photoemission spectra from $Fe_3O_4$ and the other iron oxides in the past two decades. Early studies are mostly based on the ligand-field theory[27] which interpret the photoemission features as localized 3$d$ cation levels in the oxygen ligand field[28,29]. Further studies include configuration interaction (CI) within the 3$d$ multiplet as well as charge transfer between the 3$d$ and the ligand orbitals, in order to improve the agreement with experiment and to account for the satellite features observed in photoemission[30,31]. However, these interpretations which are based on the localized-electron point of view do not take into account the anisotropy and translational symmetry of the crystal and therefore can not explain itinerant properties of the electronic structure such as band dispersion. In this regard, one earlier angle-resolved photoemission study[32] of $Fe_3O_4$(001) has found that band theory or the itinerant-electron description is more appropriate than the localized-electron point of view for describing the electronic structure of $Fe_3O_4$. Indeed, finite photoemission intensity was observed at the Fermi level which indicates that $Fe_3O_4$ is a metal, in agreement with a band structure calculation[33], although energy band dispersion as predicted by the calculation was not clearly observed.

This is confirmed by the study on the $Fe_3O_4$(111) thin film by Cai et al[20]. In **Fig. 6** the normal emission spectra taken

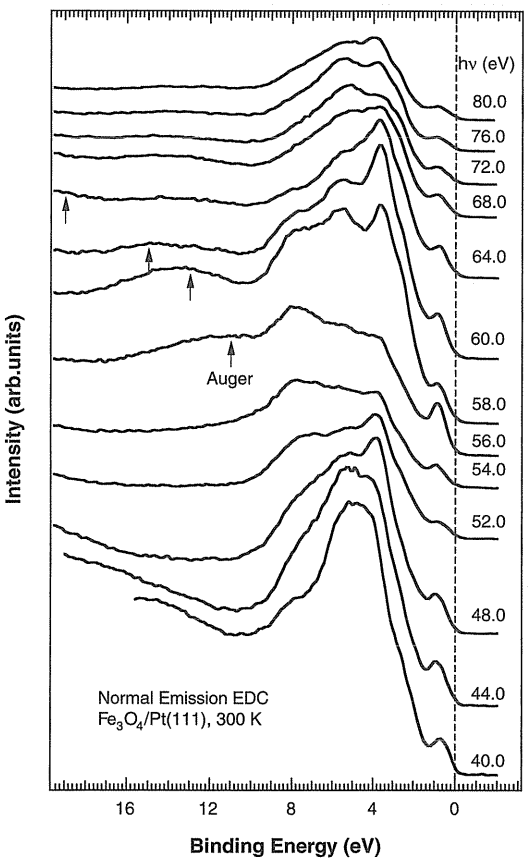


Figure 6. Normal-emission spectra from the valence bands of the $Fe_3O_4$(111) film taken at room temperature (300 K). The binding energy is measured relative to the Fermi edge of the Pt substrate. Arrows indicate the expected positions for the $M_{2,3}M_{4,5}M_{4,5}$ Auger emission for photon energies above the Fe 3$p$ excitation threshold (56 eV).

from the valence band region at room temperature (300 K) are shown. The spectra are collected using $p$-polarized light in the photon energy range of 40–80 eV which includes the Fe $3p \rightarrow 3d$ excitation threshold at 56 eV where strong resonant enhancement of photoemission is seen. The Fermi level corresponds to that of the platinum substrate. The film thickness is estimated to be about 60 Å, in which case the influence of the platinum substrate on the spectra is diminishingly small[20]. There is finite photoemission intensity at the Fermi level in all spectra, which is clearly due to the feature at the lowest binding energy and is compatible with the high conductivity of magnetite seen for bulk single crystals[32,34]. A substantial improvement compared to previous studies of bulk single crystals is the observation of clear dispersion of several distinct features in **Fig. 6**. This is attributed to the higher surface quality of the iron oxide film compared to the cleaved surfaces where the $k$-smearing caused by surface roughness is less of a problem.

A detailed study of the spectral features observed in **Fig. 6** has been carried out in the form of structure plots as shown in **Fig. 7**. Experimental points are peak or shoulder positions in the spectra determined from the local minima positions in the second derivative of the smoothed spectra. Solid lines represent direct transitions[22] between calculated valence bands and free-electron final states with an inner potential of 13.0 eV. The valence band structure used was recently calculated by Yanase and Hamada[35] who employed the full-potential linearized augmented plane wave (FLAPW) method in order to obtain the precise shape of the Fermi surface and the charge density for magnetite. Exchange and correlation energies were treated under the local spin-density approximation (LSDA) within the density functional formalism. The resulting band structure and the partial one-electron density of states agree well with two previous calculations[33,36], particularly with regard to the metallic nature of magnetite and the Fe $3d$ origin of the states located up to 1 eV below the Fermi level. In **Fig. 7**, the transition lines calculated using the majority and minority spin bands are shown separately for clarity in the left and right panels, respectively. The calculated valence bands have been shifted to higher binding energies by 0.2 eV to produce the match shown in **Fig. 7**. For the feature at $\leq 0.9$ eV binding energy,

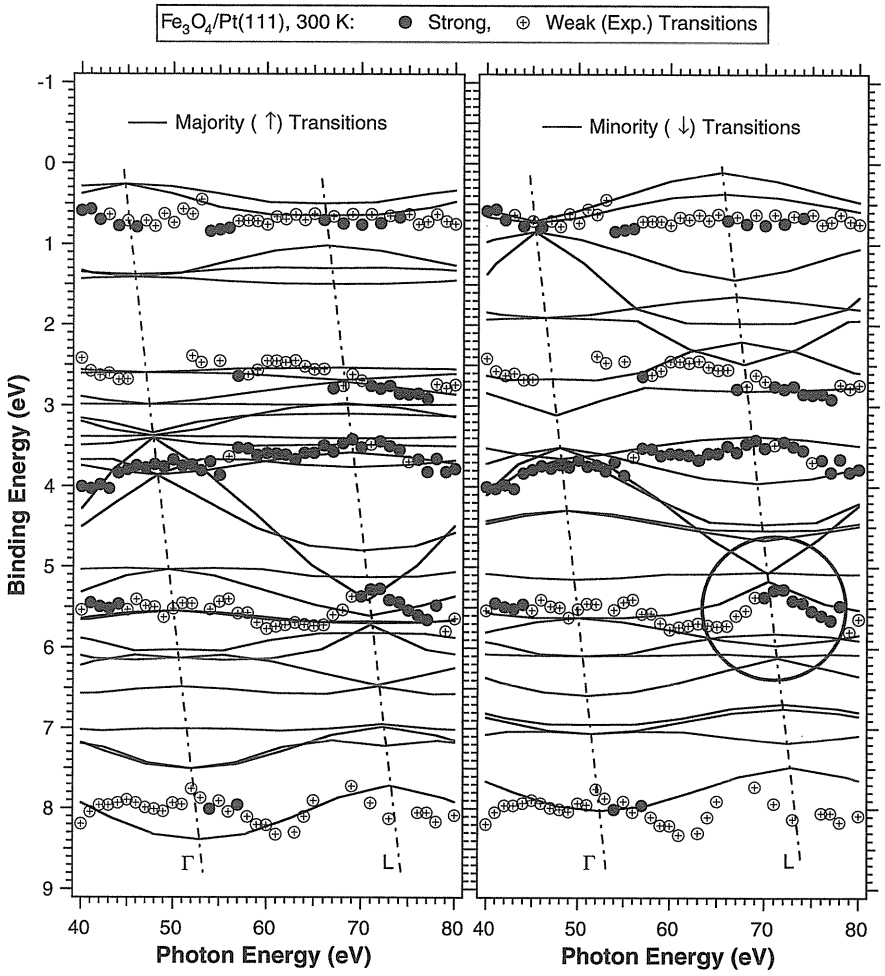


Figure 7. Structure plot for normal emission data (points) taken at 300 K. Theoretical direct transitions (solid lines) are calculated using the band structure of the majority spin (left panel) and of the minority spin (right panel) by Yanase and Hamada[35] and free-electron final states.

good agreement is found with the minority (spin-down) transitions at photon energies between 40–53 eV. In fact, this is the only possible fit since the spin polarization is found to be negative from the Fermi level down to approximately 1.7 eV at 200 K by spin-polarized photoemission[28]. Its dispersion shows a clear maximum in binding energy at around 46 eV photon energy and therefore it is identified as emission from the Γ point. The other critical point L in the symmetry line is then fixed by the calculation. Both critical points are indicated by the dash-dotted lines in **Fig. 7**. A more detailed examination of the spectra in this region, as shown in **Fig. 8**, reveals that two bands, derived from a peak and a shoulder, are present in the spectra. The two bands thus appear to correspond to the first two occupied minority-spin bands in the calculation, both of which disperse upward towards the zone boundary. Although in absolute energy terms there is still up to 0.4 eV difference between the experiment and the calculation in the critical-point energies[20], the observation of these lowest binding energy features, together with the finite intensity at the Fermi level, firmly establishes the metallic nature of magnetite and indicates that magnetite should be treated with band theory.

Agreement for the rest of the data in **Fig. 7** is less obvious. While the weak transitions are found to be associated equally well with both the majority-spin and the minority-spin bands, the strong features appear to agree better with the minority-spin transitions. This is particularly true for the strong feature around 4.0 eV for $h\nu < 56$ eV and that around 5.5 eV for $h\nu > 70$ eV These two features appear to be parts of the same calculated band which disperses downward from 3.5 eV at Γ to about 5.0 eV at the zone boundary L where a small gap opens. This band extends into the next zone and disperses to 5.5 eV at $h\nu = 80$ eV. The gap is not visible in the experimental data, but the band folding at the zone boundary (circled in **Fig. 7**) can be seen. Alternatively, a nearby majority-spin band with similar dispersion may also be assigned to these strong transitions. The energies, however, differ substantially more from those in the experiments. The comparison therefore favors the minority-spin band assignment. Since the thin film was not magnetized throughout its preparation, it is unlikely that this apparently better agreement is due to a preferential domain orientation. The problem may simply be due to some inaccuracy in the calculated band energies as indicated by the difference in the critical-point energies[20]. The actual situation may be that they contain contributions from both the majority- and minority-spin bands; a precise identification can only be achieved with spin- and angle-resolved photoemission experiments.

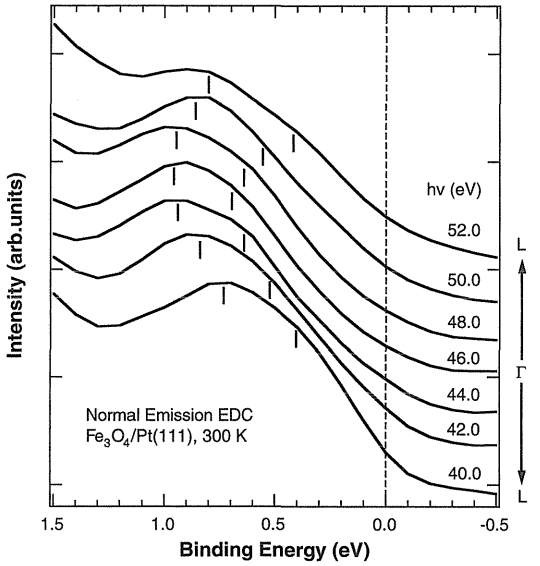


Figure 8. Normal emission spectra taken at 300 K showing the dispersion of the lowest binding energy features (indicated by the vertical bars). The turning point in the dispersion corresponds to the Γ point.

Changes in the photoemission spectra associated with the Verwey transition have also been investigated by taking data at 90 K; they are found to be quite subtle. The data has been analyzed in the same way as that at 300 K. The results are shown in **Fig. 9**. No appreciable changes are observed in the spectral region near the Fermi edge within the range of photon energies used. Chainani et al[37] have, however, reported photoemission experiments on cleaved $Fe_3O_4(110)$ surfaces and found a downwards shift of about 70 meV of the Fermi edge when their sample was cooled from 300 K to 100 K, consistent with the characteristics of the Verwey transition. In principle, one would expect the opening up of a band gap at the point where the first minority-spin band in the high temperature phase is expected to cross the Fermi level in order to explain the Verwey transition from the band structure point of view. Following the dispersion observed in **Fig. 8**, a crossing should occur at a photon energy $<40$ or $>54$ eV. However, due to the lack of data at photon energies $<40$ eV and to the interference of resonant photoemission at photon energies $>54$ eV (see below), the above possibility was not confirmed. Nevertheless, an interesting difference can be seen within the circled regions in **Fig. 7** and **9**. In the data taken at 300 K, as stated above, folded transitions from the zone boundary L are present, whereas at 90 K no such band folding is observed. The absence of folded transitions at the lower temperature is consistent with the change of the crystallographic symmetry associated with the Verwey transition[25]: the L point is no longer a Brillouin zone boundary of the monoclinic structure at low temperature.

The band dispersion discussed above is strongly interrupted by the resonant photoemission across the Fe $3p \rightarrow 3d$ excitation threshold at 56 eV, particularly of those Fe $3d$-derived bands above 4 eV binding energies. The mechanism of resonant photoemission in $3d$ transition metals and their compounds is well-known[38]. For iron oxides and other late transition-metal oxides, it is generally believed that the $3p \rightarrow 3d$ excitations are quite localized and involve only $3d$-derived states. This may therefore explain the above observation that mainly the dispersion of Fe $3d$-derived bands is affected by the resonant photoemission. Based on the same consideration, an approach has been used[31,32,34] to remove

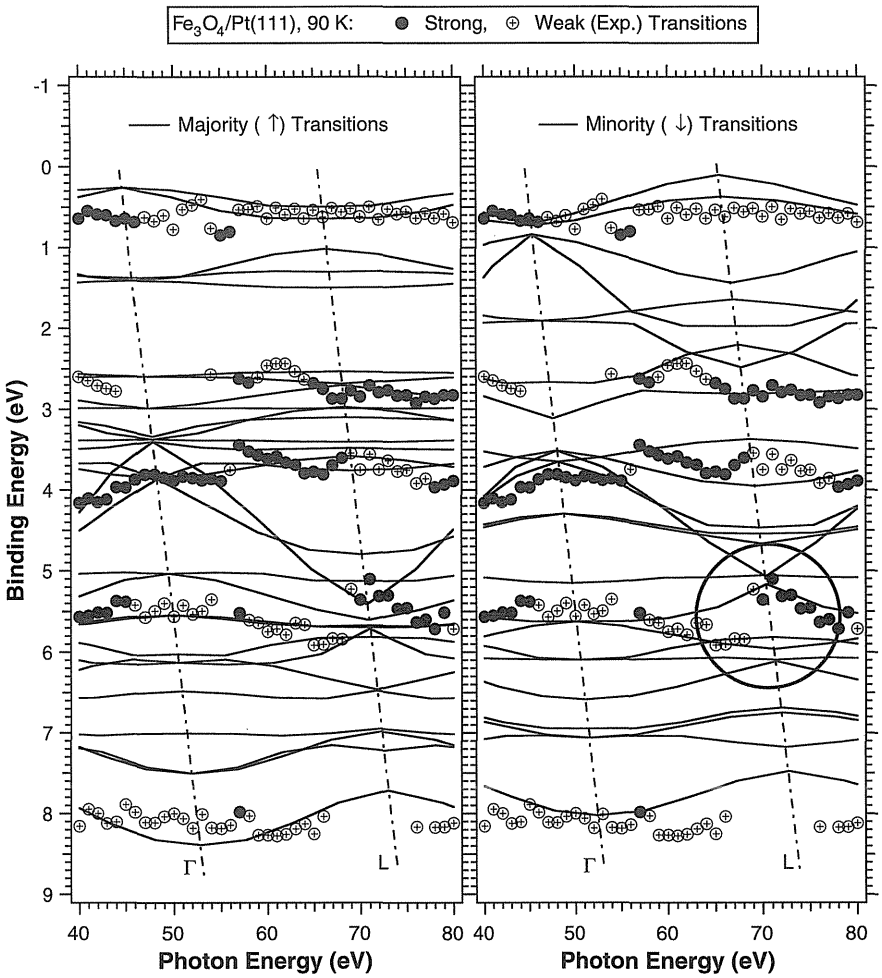


Figure 9. Same as Fig. 7 but for the normal emission data taken at 90 K.

the non-resonant O 2*p* contributions by subtracting the valence-band spectrum measured just below (off) the resonance from that just above (on) the resonance. The features of the resulting spectrum hence reflects the 3*d*-derived final states. One can investigate these final states further by measuring their resonant profiles (i.e., constant-initial-state (CIS) measurements). States of $d^{n-1}$ type usually show a typical Fano-type resonance line shape, whereas for those of $d^n \underline{L}$ ($\underline{L}$ represents a ligand hole) type an antiresonance behaviour is expected with a dip on the lower photon energy side of the Fano peak[39,40].

The difference curves and the associated CIS spectra for the $Fe_3O_4$(111) film taken at 300 K are shown in **Fig. 10** and **Fig. 11**, respectively. Three difference curves of 58 eV–53 eV, 58 eV–55 eV and 57 eV–53 eV have been constructed following the suggestions by Lad and Henrich[34] to partially separate the contributions from the $Fe^{2+}$ and $Fe^{3+}$ ions. In earlier studies[31,34] it had been observed that the on and off resonance energies depend slightly on the valency of the Fe ions in the oxides: the 58 eV–55 eV difference curve would then emphasize the contribution from the $Fe^{3+}$ ions, whereas that of 57 eV–53 eV would represent the contribution from the $Fe^{2+}$ ions. For the epitaxial $Fe_3O_4$(111) film the corresponding photon energies depend slightly on the binding energy of the resonating states and are found mostly at 58 and 53 eV[20].

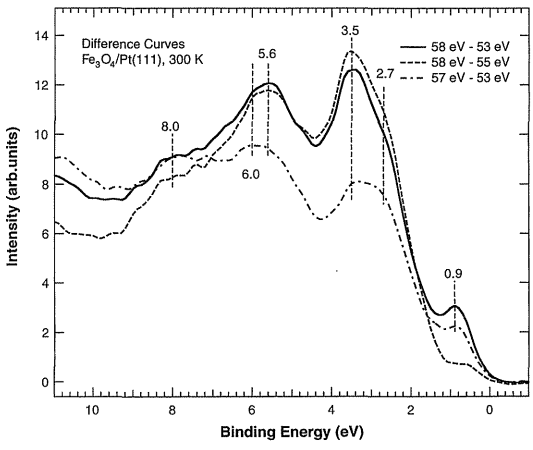


Figure 10. Difference curves for normal emission spectra taken at 300 K just above and below the Fe 3*p*→3*d* resonant photoemission.

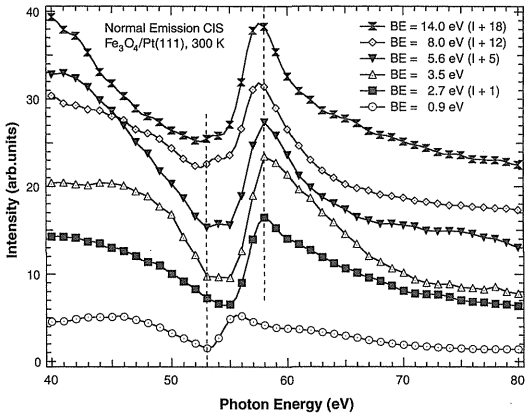


Figure 11. Normal emission constant-initial-state spectra taken at 300 K for the resonating features shown in Fig. 10 and the satellite feature at 14 eV. Vertical dashed lines mark the on- and off-resonance position.

Due to the proximity of these energies, however, Cai et al[20] has shown that in most cases the characteristics of resonant photoemission observed in FeO and $\alpha$-$Fe_2O_3$ cannot be used straightforwardly to separate contributions from the $Fe^{2+}$ and $Fe^{3+}$ ions in $Fe_3O_4$. The feature at 0.9 eV binding energy is the only exception. This feature appears in the difference curves for 58 eV–53 eV and 57 eV–53 eV, but apparently not in that for 58 eV–55 eV corresponding to the $Fe^{3+}$-related on and off resonance energies. It is therefore related only to final states of the $Fe^{2+}$ ions. This feature has been assigned in earlier studies to a state of the $d^6\underline{L}$ final-state multiplet involving charge transfer between the cation $3d$ and the ligand $2p$ orbitals[30,31]. Its resonant behavior shows a Fano line shape with an antiresonance dip (see **Fig. 11**) at 53 eV and a maximum around 55 eV. For the other resonating features in **Fig. 10**, the resonance profiles in **Fig. 11** all show a Fano-type resonance line shape with an antiresonance dip to a certain degree. This indicates that all these features are final states with a ligand hole $\underline{L}$. The satellite feature at 14 eV (see **Fig. 7**) does not have an antiresonance dip in its resonance profile and is therefore a final state of $d^{n-1}$ type.

The assignments of the above $3d$-derived final states are in essential agreement with previous resonant photoemission studies of $Fe_3O_4$(110) by Lad and Henrich[34]. It should, however, be pointed out that the binding energies of the resonating states are somewhat different from the values obtained for the $Fe_3O_4$(111) film. These differences have been attributed to crystal anisotropy and band structure effects[20]. This is because the resonant photoemission involves direct photoemission from the $3d$ levels, which is determined by the initial- and final-state band structures, and despite the Coulomb interaction in the Auger decay the wave vector remains a good quantum number.

Finally, the main features observed in **Fig. 10** are also observed in the data taken at 90 K. The spectral shapes are very similar with the main peaks around 3.5 and 5.6 eV being somewhat broader and the centers of gravity moving towards lower binding energies. These changes are likely to be caused by changes in the initial states associated with the Verwey transition. The corresponding resonance profiles reveal virtually the same behaviour for the same feature observed in the difference curves, indicating that the Verwey transition does not change the nature of the final states involved in the resonant photoemission. This demonstrates that resonant photoemission is indeed a localized process on which neither a charge ordering at the cation $B$ site nor crystallographic symmetry variations would have any noticeable effect.

## 5. Summary and Outlook

In summary, we have reviewed the current understanding of the atomic and electronic structure of the three iron oxide films, namely FeO(111), $Fe_3O_4$(111) and $\alpha$-$Fe_2O_3$(0001) epitaxially grown on a Pt(111) substrate as obtained by STM, LEED, XANES and photoemission. While the atomic surface structure of the FeO(111) film is probably well understood based on the latest STM results[14], the surface structure of the other two iron oxide films needs to be studied further. Electronically the $Fe_3O_4$(111) film is more fully understood compared to the other two oxide films. It also gives one of the examples of the role these epitaxially grown metal oxide films will likely play in the near future in contributing to our understanding of the surface and bulk electronic properties of metal oxides in general. This is in addition to the active role they will play in surface chemistry research of metal oxides which is important, for example, for understanding the principles of metal-oxide based catalysis.

## Acknowledgments

The author gratefully acknowledges fruitful collaboration with Professor A. M. Bradshaw, Dr. W. Weiss and Mr. M. Ritter throughout this project and their helpful comments on the manuscript. Thanks are also due to Professor F. Komori for his support during the writing of this review.

## References

1) V. E. Henrich and P. A. Cox: *The Surface Science of Metal Oxides* (Cambridge University Press: Cambridge, 1994).
2) H.-J. Freund, H. Kuhlenbeck and V. Staemmler: Rep. Prog. Phys. **59**, 283 (1996).
3) W. Weiss, A. B. Boffa, J. C. Dunphy, H. C. Galloway, M. B. Salmeron and G. A. Somorjai: *Adsorption on Ordered Surfaces of Ionic Solids and Thin Films*, Vol. 33, Spinger Series in Surface Science, ed. H.-J. Freund and E. Umback (Springer-Verlag: Berlin, 1993); and references therein.
4) W. Weiss, A. Barbieri, M. A. Van Hove and G. A. Somorjai: Phys. Rev. Lett. **71**, 1848 (1993); and A. Barbieri, W. Weiss, M. A. Van Hove and G. A. Somorjai: Surf. Sci. **302**, 259 (1994).
5) Th. Schedel-Niedrig, W. Weiss and R. Schlögl: Phys. Rev. B **52**, 17449 (1995).
6) D. M. Lind, S. D. Berry, G. Chern, H. Mathias and L. R. Testardi: Phys. Rev. B **45**, 1838 (1992); and references therein.
7) R. M. Jaeger, H. Kuhlenbeck, H.-J. Freund, M. Wuttig, W. Hoffmann, R. Franchy and H. Iboack: Surf. Sci. **259**, 235

(1991).
8) P. J. Chen and D. W. Goodman: Surf. Sci. **312**, L767 (1994).
9) Y. Gao, Y. J. Kim, S. A. Chambers and G. Bai: J. Vac. Sci. Technol. A **15**, 332 (1997); and references therein.
10) N. Tsuda, K. Nasu, A. Yanase and K. Siratori: *Electronic Conduction in Oxides* (Springer-Verlag: Berlin. 1991).
11) P. A. Cox: *Transition Metal Oxides. An Introduction to their Electronic Structure and Properties* (Oxford: Clarendon, 1992).
12) W. Weiss, M. Ritter, D. Zscherpel, M. Swoboda and R. Schlögl: J. Vac. Sci. Technol. A **16**, 21 (1998).
13) W. Weiss: Surf: Sci. **377-379**, 943 (1997).
14) M. Ritter, W. Ranke and W. Weiss: Phys. Rev. B **57**, 7240 (1998).
15) R. W. G. Wyckoff: *Crystal Structure*, 2nd ed., Vols. 1-3 (Krieger: Malabar, 1982).
16) H. C. Galloway, S. Sautet and M. Salmeron: Phys. Rev. B **54**, R11145 (1996).
17) C. S. Fadley, M. A. Van Hove, Z. Hussain and A. P. Kaduwela: J. Electron Spectrosc. Relat. Phenom. **75**, 273 (1995).
18) W. Weiss, M. Ritter and R. Schlügl: to be published.
19) X.-G. Wang, W. Weiss, Sh. K. Shaikhutdinov, M. Ritter, M. Petersen, F. Wagner, R. Schlögl and M. Scheffler: to be published.
20) Y. Q. Cai, M. Ritter, W. Weiss and A. M. Bradshaw: Phys. Rev. B, in press.
21) A. M. Bradshaw and J. Somers: Phys. Scr. **T31**, 189 (1990).
22) See, e.g., S. Hüfner: *Photoelectron Spectroscopy: Principles and Applications* (Springer-Verlag, Berlin, 1995).
23) E. J. Verwey, P. W. Haayman and F. C. Romeijn: J. Chem. Phys. **15**, 181 (1947).
24) P. A. Miles, W. B. Westphal and A. von Hippel: Rev. Mod. Phys. **29**, 279 (1957).
25) J. Yoshida and S. Iida: J. Phys. Soc. Jpn. **42**, 230 (1977); S. Iida: Philos. Mag. B **42**, 349 (1980).
26) D. Ihle and B. Lorenz: Philos. Mag. B **42**, 337 (1980).
27) S. Sugano, Y. Tanabe and H. Kamimura: *Multiplets of Transition-Metal Ions in Crystals* (Academic, New York, 1970).
28) S. F. Alvarado, W. Eib, F. Meier, D. T. Pierce, K. Sattler and H. C. Siegmann: Phys. Rev. Lett. **34**, 319 (1975); S. F. Alvarado, M. Erbudak and P. Munz: Phys. Rev. B **14**, 2740 (1976).
29) D. E. Eastman and J. L. Freeouf: Phys. Rev. Lett. **34**, 395 (1975).
30) P. S. Bagus, C. R. Brundle, T. J. Chuang and K. Wandelt: Phys. Rev. Lett. **39**, 1229 (1977).
31) A. Fujimori, M. Saeki, N. Kimizuka, M. Taniguchi and S. Suga: Phys. Rev. B **34**, 7318 (1986); A. Fujimori, N. Kimizuka, M. Taniguchi and S. Suga: Phys. Rev. B **36**, 6691 (1987).
32) K. Siratori, S. Suga, M. Taniguchi, K. Soda, S. Kimura and A. Yanase: J. Phys. Soc. Jpn. **55**, 690 (1986).
33) A. Yanase and K. Siratori: J. Phys. Soc. Japan **53**, 312 (1984).
34) R. J. Lad and V. E. Henrich: Phys. Rev. B **39**, 13479 (1989); and J. Vac. Sci. Technol. A **7**, 1893 (1989).
35) A. Yanase and N. Hamada: to be published; and A. Yanase, ISSP Diaries (in Japanese) **37**, 66 (1997).
36) Z. Zhang and S. Satpathy: Phys. Rev. B **44**, 13319 (1991).
37) A. Chainani, T. Yokoya, T. Morimoto and T. Takahashi: Phys. Rev. B **51**, 17976 (1995).
38) For a review, see, L. C. Davis: J. Appl. Phys. **59**, R25 (1986).
39) L. C. Davis: Phys. Rev. B **25**, 2912 (1982).
40) A. Fujimori and F. Minami: Phys. Rev. B **30**, 957 (1984).